Adaptive Kalman Filter Based on Online ARW Estimation for Compensating Low-Frequency Error of MHD ARS

Yunhao Su, Junfeng Han, Caiwen Ma, Jianming Wu, Xuan Wang, Qinghua Zhu, and Jie Shen

Abstract—**Magnetohydrodynamic angular rate sensor (MHD ARS) can precisely detect angular vibration information with a bandwidth of up to one kilohertz. However, due to secondary flow and viscous force, it experiences performance degradation when measuring low-frequency angular vibrations. This article presents an adaptive Kalman filter that uses online angular random walk (ARW) estimation to correct for the low-frequency error of MHD ARS, where a microelectromechanical system (MEMS) gyroscope is used to measure low-frequency vibrations. The proposed algorithm determines the signal frequency based on the ARW coefficients and adjusts the measurement noise covariance to achieve accurate fusion results. Thus, the method solves the problem of frequency-dependent variation of the amplitude response of the sensors in data fusion. Initially, the algorithm calculates the ARW coefficient recursively utilizing the measurement signals of both sensors. Then, the operational frequencies of both sensors are determined by analyzing the correlation between the ARW coefficient and frequency. Subsequently, in the Sage-Husa adaptive Kalman filter (SHAKF), the Kalman gain matrix is adjusted by modifying the measurement noise variances of both sensor signals individually. Moreover, the stability of the proposed algorithm is achieved by introducing an adaptive matrix to constrain the measurement noise covariance estimation. In the experiment, the fusion effects of single-frequency and mixed-frequency signals are tested separately. The experimental results show that for frequency variation and frequency mixing, the proposed algorithm in this study significantly improves the fusion results.**

Index Terms—**Angular random walk (ARW), magnetohydrodynamic angular rate sensor (MHD ARS), microelectromechanical system (MEMS) gyroscope, Sage-Husa adaptive Kalman filter (SHAKF), signal fusion.**

I. Introduction

IN DEEP space exploration, some projects require very stable laser links, so the requirements for pointing and aiming the laser beam are increasing. High-precision aiming is essential for laser links in free-space laser communication [1] and gravitational wave detection [2]. There are usually two main factors that interfere with the aiming stabilization of the laser link. The first is atmospheric turbulence [3], which affects the density of the transmission medium of the laser link and causes refraction of the laser. This phenomenon occurs in the laser link between the ground-based terminal and the on-orbit terminal. The second factor involves mechanical vibrations that result from the various components of the satellite platform during its operational phase, such as the harmonic vibration produced by the solar panel or reaction wheel [4]. Typically, the amplitude of the high-frequency mechanical vibration varies from a few to several tens of microradians. The vibration frequency spectrum ranges from zero to several hundred Hz. Mechanical vibrations can disrupt the pointing position of the laser beam and negatively affect the stability of the laser link.

The measured vibration information can be used for feedforward compensation in the control system, effectively suppressing laser jitter. At present, attitude sensors commonly used on satellite platforms include sun sensors, gyroscopes, and star trackers. These sensors typically operate within frequency ranges of a few to tens of Hz [5]. The ability of the optical system to actively suppress laser beam jitter is limited by its inability to detect high-frequency microvibrations. Magnetohydrodynamic angular rate sensor (MHD ARS) has an operational bandwidth of kilohertz and measurement accuracy on the order of nanoradians [6]. It is also characterized by small size, lightweight, durability, and no mechanical loss. MHD ARS has been applied to various high-precision optical pointing and aiming systems, such as the Lunar Laser Communication Terminal [7], [8] and the Mars Laser Communication Terminal [9]. However, because of secondary flow and viscous force, the response of MHD ARS decreases in the low-frequency range (<2 Hz) [10].

Combining MHD ARS with a low-frequency attitude sensor, such as a microelectromechanical system (MEMS) gyroscope, is one method of compensating for its low-frequency error. MEMS gyroscopes are small, lightweight, and can meet the measurement of low-frequency and large-magnitude vibration of satellite platforms. Therefore, it meets the development direction of miniaturization and lightweight

laser communication terminals. To achieve data fusion, new methods are constantly being proposed. Iwata et al. [11] proposed to obtain wide-bandwidth attitude information by fusing the measurement signals from a star tracker, gyroscopes, and a MHD angular displacement sensor on the Advanced Land Observing Satellite using a Kalman filter. Usually, the classical Kalman filter is a simple and feasible algorithm of signal fusion. However, the statistical properties of its measurement noise remain constant while the system model may be inaccurate, resulting in error. Therefore, the classical Kalman filter encounters challenges in signal fusion for complex multisignals. Sun et al. [12] proposed a data fusion method based on extended Kalman filtering for star trackers and MEMS gyroscopes, which realizes the mutual compensation of the accuracy of the two sensors. Liang et al. [13] proposed a nested Kalman fusion-based method for data fusion of MEMS gyroscopes to optimize the Allan variance results. The Sage-Husa adaptive Kalman filter (SHAKF) enables on-line updating of the statistical properties of the noise by recursively calculating the variances of both measurement and system noise [14]. However, it should be noted that satellite platforms have a wide frequency range of vibration and sensors have different measurement frequency ranges. The change in vibration frequency will cause each sensor to produce different response results, such as the attenuation of the response of the MHD ARS at low frequencies and the MEMS gyroscope at high frequencies. The system needs to adjust the filter according to the change in the signal frequency to cope with the change in the different measurement signals.

In this article, an adaptive Kalman filter based on online angular random walk (ARW) estimation is proposed. First, the algorithm utilizes the measurement signals to iteratively calculate the ARW coefficients of both MHD ARS and MEMS gyroscopes. Then, the frequency of the measurement signal is determined by analyzing the relationship between the ARW coefficient and frequency. Next, the main diagonal elements of the measurement noise covariance matrix are modified, respectively, to adjust the Kalman gain. This changes the degree of trust that the filter places in the measurement signals of both sensors, respectively. As a result, it will adjust the operation of the SHAKF algorithm to ensure accuracy. Finally, the introduction of an adaptive matrix for the measurement noise covariance matrix estimation enhances the stability of the proposed algorithm.

The low-frequency response attenuation of MHD ARS is analyzed in Section II, the details of the proposed algorithm are presented in Section III, the experimental results are presented in Section IV, and the effect of the proposed algorithm and conclusion obtained from the experiment are summarized in Section V.

II. MHD ARS Low-Frequency Error Analysis

The basic principle of MHD ARS is shown in Fig. 1. The conducting fluid fills the space between the inner and outer tubes. The permanent magnet in the inner tube forms a magnetic field $\boldsymbol{B}$ perpendicular to the sensitivity axis. When the annular channel generates an angular rate $\boldsymbol{v}$ around the sensitive axis, the conducting fluid will remain in place due
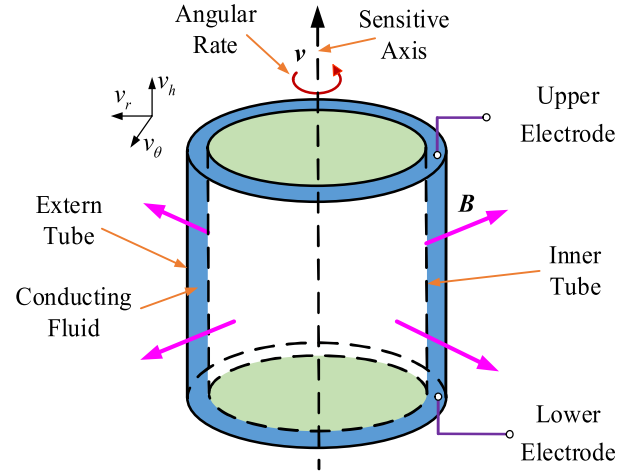

Fig. 1. Schematic of the principle of MHD ARS.

to the low friction between the tube surface and the fluid, as well as the high inertia of the conducting fluid. In this case, the conducting fluid generates a relative angular rate to the magnetic field $\boldsymbol{B}$. The conducting fluid incises the magnetic flux, and the upper and lower electrodes generate an induced electromotive force [15].

Assuming a constant density of the fluid and a uniform magnetic field, the conducting fluid motion of the above process satisfies the following equation [16]:

$$\begin{cases} \rho\left[\dfrac{\partial \boldsymbol{v}}{\partial t} + (\boldsymbol{v} \cdot \nabla)\boldsymbol{v}\right] = \rho\boldsymbol{g} - \nabla P + \dfrac{1}{\mu}(\boldsymbol{B} \cdot \nabla)\boldsymbol{B} + \mu_f \nabla^2 \boldsymbol{v} \\ \dfrac{\partial \boldsymbol{B}}{\partial t} = \nabla \times (\boldsymbol{v} \times \boldsymbol{B}) + \dfrac{1}{\mu\sigma}\nabla^2 \boldsymbol{B} \end{cases}$$

$$(1)$$

where $\boldsymbol{v} = (v_r, v_\theta, v_h)$ is the fluid velocity vector, in (r, θ, h). r is the radial direction, h is the axial direction, and θ is the circumferential direction. ρ is the conducting fluid density, $\boldsymbol{g}$ is the gravity, P is the total pressure, μ is the magnetic permeability, μ_f is the dynamic viscosity coefficient, σ is an electrical conductivity.

$v_\theta \gg v_r \sim O[0]$, $v_\theta \gg v_h \sim O[0]$, O means the two equations in the same order of magnitude. Assume that v_θ is linearly dependent on r, the motion of the conducting fluid in that direction can be simplified as

$$\frac{\partial v_\theta}{\partial t} = -\frac{\sigma B_r^2 u_\theta}{\rho} + \eta_f \frac{\partial^2 v_\theta}{\partial h^2} \qquad (2)$$

where σ is an electrical conductivity. $u_\theta = v_\theta - v$ is the relative velocity. $\eta_f = \mu_f / \rho$ is the kinematic viscosity coefficient.

The induced electromotive force E is proportional to the integral of the difference between the fluid velocity and the fluid channel velocity in the axial direction h. E can be simplified as follows:

$$E(t) = \frac{k}{l} \int_0^l u_\theta \, dh \qquad (3)$$

where k is the ratio of the induced electromotive force E to the relative velocity between the fluid and the channel and l is the height of the annular channel.
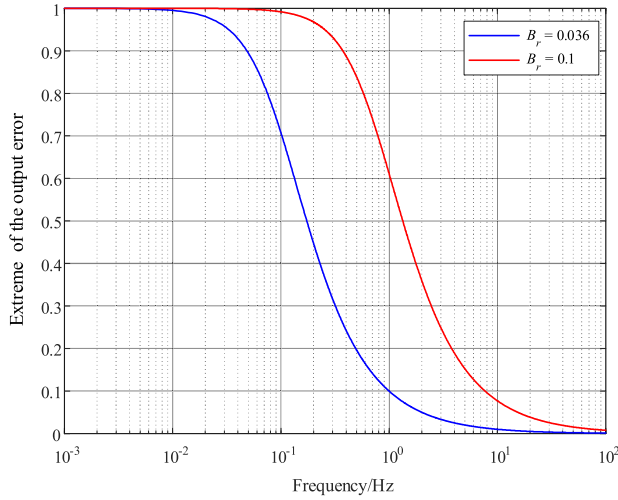
Fig. 2.   Error extreme e_M variation curve with frequency.

Assuming $v = \sin(\omega t)$, $\omega = 2\pi f$, f is the angular rate frequency, then it can be calculated that E is

$$E(t) = K\left[\frac{\omega^2}{\omega^2 + (\pi^2\eta_f/l^2 + \sigma B_r^2/\rho)^2}\sin(\omega t)\right.$$
$$\left. + \frac{\omega(\pi^2\eta_f/l^2 + \sigma B_r^2/\rho)}{\omega^2 + (\pi^2\eta_f/l^2 + \sigma B_r^2/\rho)^2}\cos(\omega t)\right] \quad (4)$$

where $K = 8k/\eta_f\pi^2$ is the scale factor of the sensor.

The output error is expressed as follows:

$$e(t) = \frac{1}{K}E(t) - v(t) = \frac{\omega(\pi^2\eta_f/l^2 + \sigma B_r^2/\rho)}{\omega^2 + (\pi^2\eta_f/l^2 + \sigma B_r^2/\rho)^2}\cos(\omega t)$$
$$- \frac{(\pi^2\eta_f/l^2 + \sigma B_r^2/\rho)^2}{\omega^2 + (\pi^2\eta_f/l^2 + \sigma B_r^2/\rho)^2}\sin(\omega t). \quad (5)$$

The extreme e_M is obtained by taking the derivative of the error with respect to time t

$$e_M(\omega) = \frac{\pi^2\eta_f/l^2 + \sigma B_r^2/\rho}{\sqrt{\omega^2 + (\pi^2\eta_f/l^2 + \sigma B_r^2/\rho)^2}}. \quad (6)$$

Assuming $B_r = 0.036$ T and using mercury as the conducting fluid, then $\eta_f\pi^2/l^2 + \sigma B_r^2/\rho \approx 0.1$. The blue line in Fig. 2 shows the trend of the e_M with frequency. If $B_r = 0.1$ T, as shown by the red line in Fig. 2, the low-frequency performance becomes worse. The curves show that the extreme e_M of the output error increases as the frequency of the input angular rate decreases.

III. IMPROVED ALGORITHM PRINCIPLE

A. Sage-Husa Adaptive Filter and Signal Fusion

The SHAKF consists of a mutually coupled Kalman filter and the Sage-Husa noise estimator. The Kalman filter is a linear minimum variance filter based on the original signal characteristics, and the Sage-Husa noise estimator is a suboptimal unbiased extremely large a posteriori estimator that can estimate the noise statistics online [17].

The equations of state and measurement of both MHD ARS and MEMS gyroscope can be expressed as follows:

$$\begin{cases} \dot{x} = Ax + Bx_1 + \delta \\ z = Hx + \varepsilon \end{cases} \quad (7)$$

where x_1 is the true angular rate, δ is the system noise, and ε is the measurement noise.

The steps of the SHAKF are as follows.
1) Update the state estimation

$$\hat{X}_{k,k-1} = A\hat{X}_{k-1} + Bx_1. \quad (8)$$

2) Update the state error covariance matrix estimation

$$P_{k,k-1} = AP_{k-1,k-1}\ A^T + \hat{Q}_k. \quad (9)$$

3) Calculate the Kalman gain

$$K_k = P_{k,k-l}H^T(HP_{k,k-1}H^T + \hat{R}_k)^{-1}. \quad (10)$$

4) Calculate the innovation covariance matrix

$$e_k = Z_k - H\hat{X}_{k,k-1} - r_k. \quad (11)$$

5) Update the state estimation

$$\hat{X}_k = \hat{X}_{k,k-1} + K_ke_k. \quad (12)$$

6) Update the error covariance

$$P_k = (I - K_kH)P_{k,k-1}. \quad (13)$$

7) Sage-Husa noise estimation

$$\hat{q}_k = (1-d_k)\hat{q}_{k-1} + d_k(\hat{X}_{k,k} - A\hat{X}_{k-1,k-1}) \quad (14)$$
$$\hat{Q}_k = (1-d_k)\hat{Q}_{k-1} + d_k(K_ke_ke_k^TK_k^T - AP_{k-1,k-1}\ A^T) \quad (15)$$
$$\hat{r}_k = (1-d_k)\hat{r}_{k-1} + d_k(Z_k - H\hat{X}_{k,k-1}) \quad (16)$$
$$\hat{R}_k = (1-d_k)\hat{R}_{k-1} + d_k(e_ke_k^T - HP_{k,k-1}H^T) \quad (17)$$

where $d_k = (1-\beta)/(1-\beta^{k+1})$, β is the forgetting factor.

The state and measurement equations for MHD ARS and MEMS gyroscope are as follows:

$$\begin{cases} \dot{X} = AX + \delta \\ Z = HX + \varepsilon \end{cases} \quad (18)$$

$$X = \begin{bmatrix} x_1 & x_{gyro} & x_{MHD} \end{bmatrix}^T, Z = \begin{bmatrix} z_{gyro} & z_{MHD} \end{bmatrix}^T \quad (19)$$

$$A = \begin{bmatrix} 0 & 0 & 0 \\ B_{gyro} & A_{gyro} & 0 \\ B_{MHD} & 0 & A_{MHD} \end{bmatrix}, \quad H = \begin{bmatrix} H_{gyro} & H_{MHD} \end{bmatrix}^T. \quad (20)$$

In general, the sampling rate of MEMS gyroscope is lower than that of MHD ARS, so the update sequence of SHAKF can be shown in Fig. 3.
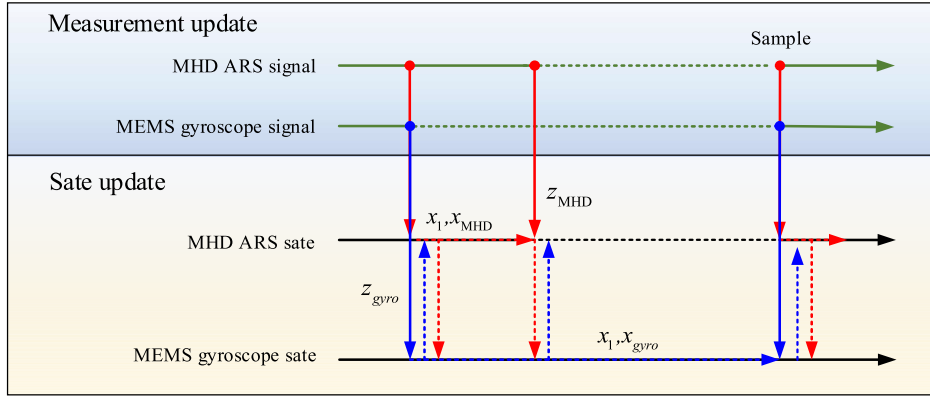
Fig. 3.   SHAKF update sequence.

B. Principle of Online Frequency Analysis

According to the linear system theory, ARW, bias instability (BI), and angular rate random walk (ARRW), these three types of noise can be described by the following model [18]:

$$y_{ARW}(k) = (N/\Delta T) \cdot u_{ARW}(k) \tag{21}$$

$$y_{BI}(k) = (1 - \beta \Delta T) y_{BI}(k-1) + \beta B \sqrt{\Delta T} \cdot u_{BI}(k) \tag{22}$$

$$y_{ARRW}(k) = y_{ARRW}(k-1) + K \sqrt{\Delta T} \cdot u_{ARW}(k) \tag{23}$$

where u_{ARW}, u_{BI}, and u_{ARRW} are the independent Gaussian white noise.

Then state and measurement equations can be written as follows:

$$z(k) = \begin{bmatrix} 1 & 1 \end{bmatrix} \times \begin{bmatrix} y_{ARRW}(k) \\ y_{BI}(k) \end{bmatrix} + \frac{N}{\sqrt{\Delta T}} \cdot u_{ARW}(k). \tag{24}$$

According to the results of the Allan variance, MHD ARS contains two main types of random noise: ARW and BI [19]. After filtering out the BI using methods like de-averaging, the noise primarily consists of the ARW characteristics. Based on the properties of variance, the ARW coefficient N can be expressed as follows:

$$N = \sqrt{R \cdot \Delta T} \tag{25}$$

where R is noise variance and ΔT is sampling time.

The process of calculating Allan variance is equivalent to different bandpass filters at different correlation times, and therefore, can analyze different noise terms. The quantization noise is uniformly distributed in the frequency band, so when the sampling frequency is increased, the energy of the quantization noise does not change, while the range of the noise distribution in the frequency domain increases. This means that the quantization noise decreases significantly when the sampling rate is increased [18]. When the correlation time τ_M is equal to the sampling period, the result of the Allan variance estimator can be approximated as the variance of the quantization noise at the current moment, and the quantization noise term is reduced in this measurement variance

$$R_k \approx \hat{\sigma}_k^2(\tau_M) \tag{26}$$

$$\hat{\sigma}_k^2(\tau) = \frac{1}{2(N-1)} \sum_{i=2}^{k} \left(\bar{\Omega}_i(\tau) - \bar{\Omega}_{i-1}(\tau) \right)^2 \tag{27}$$

where $\bar{\Omega}_i(\tau)$ is a sample of the average angular rate.

In the SHAKF, only the shortest correlation time is calculated, that is, the correlation time of the Allan variance is the sampling time. Then the Allan variance at the current moment can be expressed as the following equation:

$$\hat{\sigma}_k^2(\tau_0) = \left(1 - \frac{1}{k-1} \right) \left[\frac{1}{2(k-2)} \sum_{i=2}^{k-1} (Z_i - Z_{i-1})^2 \right] + \frac{1}{2(k-1)} (Z_k - Z_{k-1})^2. \tag{28}$$

The update of the measurement noise variance can be written in the following form [18]:

$$R_k = \left(1 - \frac{1}{k-1} \right) R_{k-1} + \frac{1}{2(k-1)} (Z_k - Z_{k-1})^2. \tag{29}$$

Therefore, the ARW coefficient N_k at the current moment can be calculated recursively. The N_k is a physical quantity that is related to the measurements at both the current and historical moments

$$N_k = \left(1 - \frac{1}{k-1} \right) N_{k-1} + \frac{\Delta T}{2(k-1)} (Z_k - Z_{k-1})^2. \tag{30}$$

The Allan variance is represented in the frequency domain as

$$\sigma^2(\tau) = 4 \int_0^{+\infty} S_\Omega(f) \frac{\sin^4(\pi f \tau)}{(\pi f \tau)^2} d(f) \tag{31}$$

where $S_\Omega(f)$ is the power spectral density of the signal. The Allan variance is related to the statistical properties of the stochastic process inherent in MHD ARS. In other words, it is related to the power spectral density of the noise in the measurement data of MHD ARS under stationary conditions. If the angular rate is constant, the Allan variance remains unchanged. However, when the angular rate varies, additional power spectral components are induced, resulting in changes to the Allan variance result.

When MHD ARS measures harmonic vibration, the angular rate is $v = 2a\pi f \cdot \cos(2\pi f t)$, and a is the angular amplitude. Equation (32) can be expressed in the following form:

$$N_k = \left(1 - \frac{1}{k-1} \right) N_{k-1} + \frac{\Delta T a \pi f}{k-1} \{ \cos[2\pi f t] - \cos[2\pi f (t - \Delta T)] \}^2. \tag{32}$$
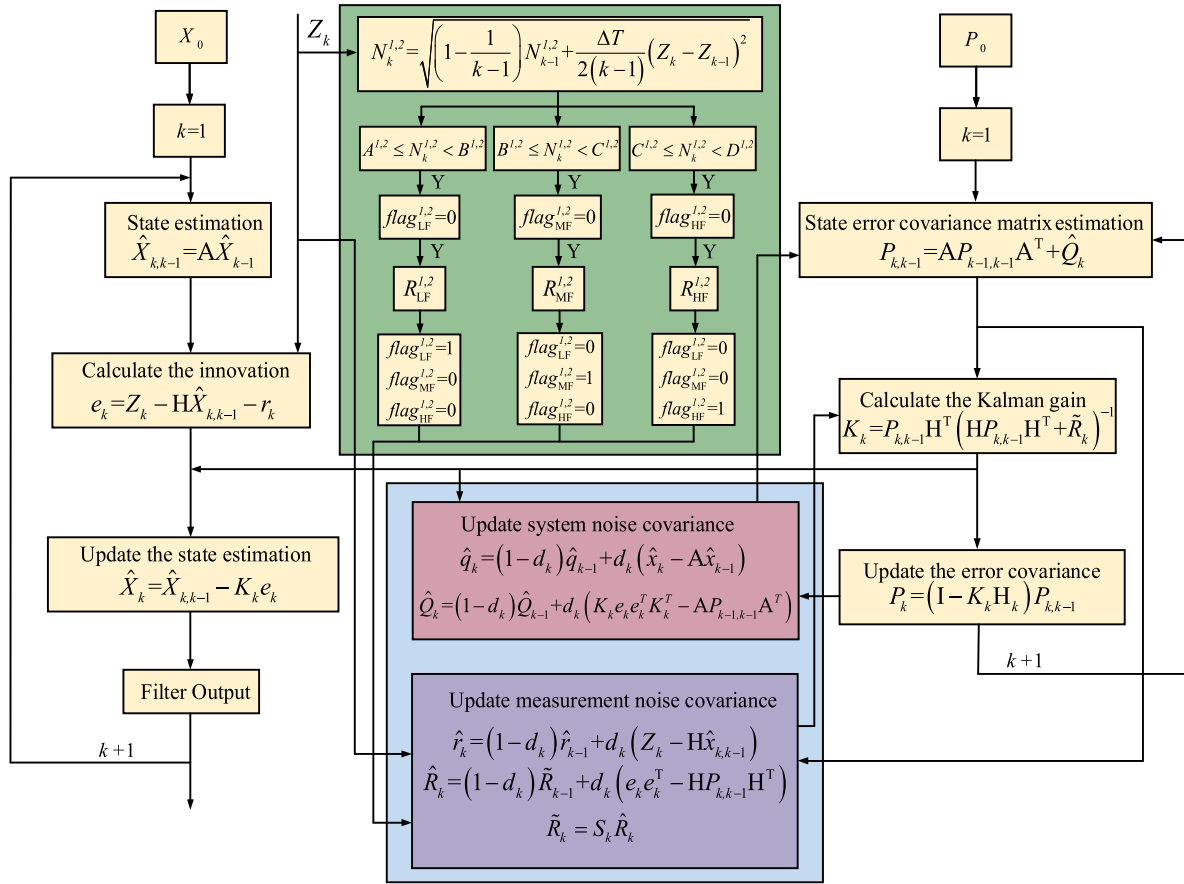
Fig. 4. SHAKF flow based on online frequency analysis.

When the amplitude, current moment, and sampling time are certain, if the angular rate frequency f is larger, the value of the second part will be larger. Therefore, in the SHAKF, the iteration results of the N_k can be used to determine the operational frequency.

In the proposed algorithm, the measurement noise covariance matrix $\hat{R}_k$ is modified according to the relationship between the N_k and frequency. Since the update of the N_k relies only on measurements, its recursive estimation and the Sage–Husa noise estimator are uncoupled. This ensures the reliability of determining frequency.

The output signals of MHD ARS and MEMS gyroscope can be divided into three frequency bands by the variation of the N_k. The performance of MHD ARS is attenuated in the low-frequency range, so the filter must rely on the MEMS gyroscope measurement signal. The filter uses a low-noise, high-accuracy MHD ARS measurement signal in the mid-frequency range where the frequency responses of the two sensors overlap. The MEMS gyroscope is ineffective in the high-frequency range, so the filter must trust the MHD ARS measurement signal.

C. Adaptive Matrix for Measurement Noise Covariance

The update of the measurement noise variance estimation has a significant impact on the performance of the SHAKF. Adjustment of the measurement noise covariance matrix in a change in the update of its estimate may reduce the efficiency of the filter or even lead to divergence. If the

SHAKF is working well, the theoretical value of the innovation covariance matrix satisfies the following equation:

$$C_k = E\left[e_k^{\mathrm{T}} e_k\right] = \mathrm{H} P_{k,k-1} \mathrm{H}^{\mathrm{T}} + \hat{R}_k. \tag{33}$$

When the system and measurement noise are uncorrelated Gaussian noise, the optimal estimate for the maximum likelihood of the innovation covariance matrix is given by the following equation [20]:

$$\hat{C}_k = \frac{1}{n} \sum_{j=j_0}^{k} \left(Z_k - \mathrm{H}\hat{X}_{k,k-1}\right)_j \left(Z_k - \mathrm{H}\hat{X}_{k,k-1}\right)_j^{\mathrm{T}} \tag{34}$$

where n is the sliding window, $j_0 = k - n + 1$. The innovation covariance matrix estimate and the theoretical value are satisfied when the prediction results of the previous moment deviates from the current observation

$$\hat{C}_k \geq \mathrm{H} P_{k,k-1} \mathrm{H}^T + \hat{R}_k. \tag{35}$$

When adjusting the measurement noise covariance, the adjustment should be limited based on the results of the state estimation to ensure the stability of the filter. A possible approach is to adjust the measurement noise covariance $\hat{R}_k$ and, if necessary, reduce the influence of the measurements Z_k on the filtering results by introducing an adaptive matrix. The adaptive matrix S_k is introduced

$$\tilde{R}_k = S_k \hat{R}_k \tag{36}$$

$$S_k > \tilde{R}_k \left(\hat{C}_k - \mathrm{H} P_{k,k-1} \mathrm{H}^{\mathrm{T}}\right)^{-1}. \tag{37}$$

TABLE I
EQUIPMENT LIST AND PARAMETERS OF THE EXPERIMENTAL PLATFORM

| Equipment	Model	Parameter
MHD ARS	SX300	Angular rate range: $\pm30°$/s Bandwidth:2-1000Hz Analog output:±10V Measurement accuracy:1×10^{-5}°/s
MEMS gyroscope	ADIS16505	Angular rate range:$\pm500°$/s Sensitivity: 2,621,440 LSB/°/s Digital signal output frequency:2kHz Output Noise (Filtering): 0.045°/s(rms)
DSP	TMS320F28335	System clock frequency:150MHz
Analogue-to-digital conversion	ADC7606	Minimum voltage resolution:0.076mV Sampling rate:20kHz
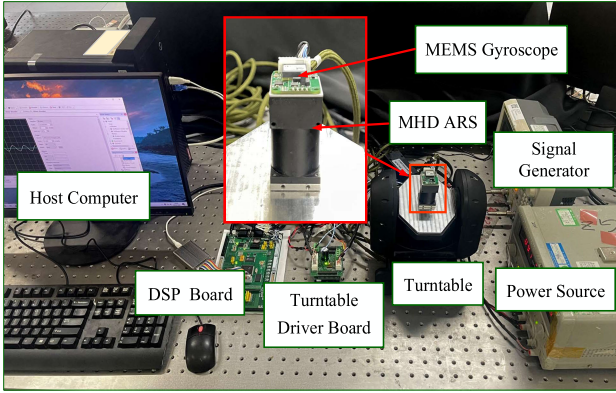
Fig. 5.   Experimental platform.

To ensure that the S_k is a nonnegative diagonal matrix, the S_k is set to be an adaptive matrix with main diagonal elements greater than 1

$$S_k = \max\left[1, \alpha\hat{C}_k / \left(\mathrm{H}P_{k,k-1}\mathrm{H}^{\mathrm{T}} + \hat{R}_k\right)\right] \tag{38}$$

where $\alpha < 1$ is the regulating factor.

The complete algorithm flow is shown in Fig. 4. The green frame contains the online frequency analysis method, as described in the previous section, which uses the update of the $N_k^{1,2}$ to determine the frequency of both sensors, where 1 represents MHD ARS and 2 represents MEMS gyroscope. In this process, six flags are set, which are the low-frequency flag $flag_{\mathrm{LF}}^{1,2}$, the mid-frequency flag $flag_{\mathrm{MF}}^{1,2}$, and the high-frequency flag $flag_{\mathrm{HF}}^{1,2}$.

When the value of the $N_k^{1,2}$ satisfies $[A^{1,2}, B^{1,2})$, it is determined that MHD ARS or MEMS gyroscope is operating in the low-frequency band, and measurement noise variance is adaptively set to the $R_{\mathrm{LF}}^{1,2}$ allowing the measurement signal from the MEMS gyroscope to be effectively utilized. The $flag_{\mathrm{LF}}^{1,2}$ is set to 1, at the next moment, the $\hat{R}_k$ is updated only in the Sage-Husa noise estimator, as shown by the blue frame in Fig. 4. The principle is the same for the other two operational bands. Therefore, the filter can determine the operational bands of both sensors at the next moment. The ARW coefficients of both sensors are iterated independently,

ensuring that the filter can still determine the operational frequency of each sensor when measuring mixed signals.

IV. EXPERIMENTAL RESULTS AND ANALYSIS

A. Experimental Platform

To verify the effectiveness of the proposed algorithm, we use the angular vibration provided by the turntable to simulate the narrow-band harmonic vibration of the satellite platform. The experimental platform is shown in Fig. 5. Table I provides information on the names and specific parameters of the devices in the experimental platform.

As shown in Fig. 5, to avoid the interference of mechanical vibrations in the environment, the turntable was mounted on an air-floating stabilized platform. We mounted the MEMS gyroscope directly above the MHD ARS so that their sensitive axes are parallel to ensure the consistency of the two measurements of angular rate. The sampling rate of the MHD ARS is 20 kHz and that of the MEMS gyroscope is 2 kHz. The algorithms are executed using the digital signal processing (DSP) board, and the data are obtained from the host computer.

B. Measurement Models of Sensors

In this work, we obtained the frequency response points of both sensors using the single-point frequency sweep method. The angular rate amplitude is 1°/s. Due to the limitations of the turntable, we were unable to acquire all response points within the operational bandwidth of the MEMS gyroscope and MHD ARS. Considering the frequency characteristics of both sensors, it can be inferred that the MEMS gyroscope functions as a low-pass filter while the MHD ARS operates as a high-pass filter.

Their transfer functions can be expressed as the following equation:

$$G_{\mathrm{gyro}} = \frac{as + b}{cs^2 + ds + e}, \quad G_{\mathrm{MHD}} = \frac{gs}{ms^2 + ns + o}. \tag{39}$$

According to the frequency response points, the values of the constants in the transfer functions can be determined, where $a = 154.537$, $b = 15.626$, $c = 5.2175$, $d = 148$,
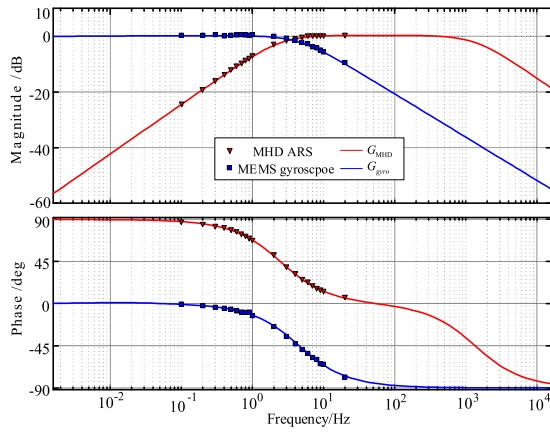
Fig. 6.   Frequency response curve of the sensors.

Fig. 7.   ARW coefficient online estimation results with frequency variation curve.

$e = 15.444$, $g = 2200$, $m = 0.255$, $n = 2178$, $o = 33900$. The frequency response points and transfer functions frequency response curves are shown in Fig. 6. The trends of the transfer function frequency response curves coincide with the frequency response points so that the transfer functions can be converted into the form of a state equation, as in (20).

C. Online Frequency Analysis

In this work, to determine the relationship between the ARW coefficients of the MHD ARS and the MEMS gyroscope with respect to the angular rate frequency, we chose a frequency range from 0.1 to 25 Hz with an angular rate amplitude of 1°/s. The results are shown in Fig. 7.

The online estimation results of the ARW coefficients for both sensors increase as the signal frequency increases. Therefore, it is feasible to use ARW coefficient estimation to determine the signal frequency.

D. Single-Frequency Signal Experiment

In this test, we chose three single frequencies: 0.5, 4, and 10 Hz, with an angular rate amplitude of 1°/s. Where 0.5 Hz is the operational frequency of the MEMS gyroscope; 4 Hz serves as the operational frequency for both sensors; and 10 Hz represents the operational frequency of the MHD ARS. The three frequencies cover the bands where the amplitude response of both sensors is smooth and attenuated.

The fusion results of the proposed algorithm are displayed in Figs. 8–10. The proposed algorithm trusts the MEMS gyroscope measurement signal more when measuring the 0.5 Hz signal and reduces the utilization of the MHD ARS attenuation measurement signal. However, due to the low sampling rate and high noise of the MEMS gyroscope, there is a significant error in the fused signal. From Figs. 9 and 10, it is obvious that the proposed algorithm relies more on the measurement signals of the MHD ARS, and the fusion results are smoother and produce fewer errors. The fusion results of the three frequency signals demonstrate that the proposed algorithm successfully utilizes the online estimated ARW coefficient to determine the frequency of the signal. The fusion results can be significantly improved by adjusting the degree of trust that the filter places in the measurement signal from both sensors.
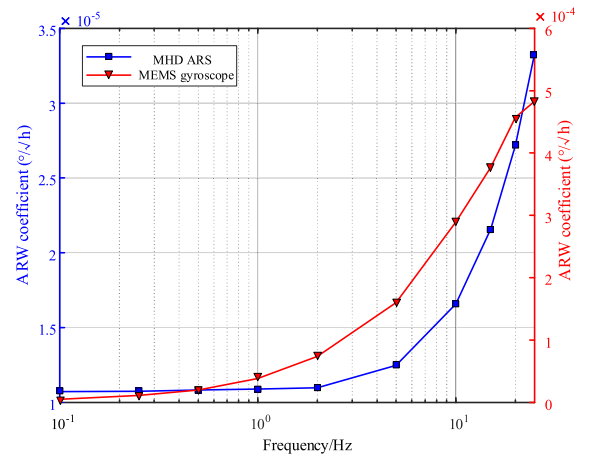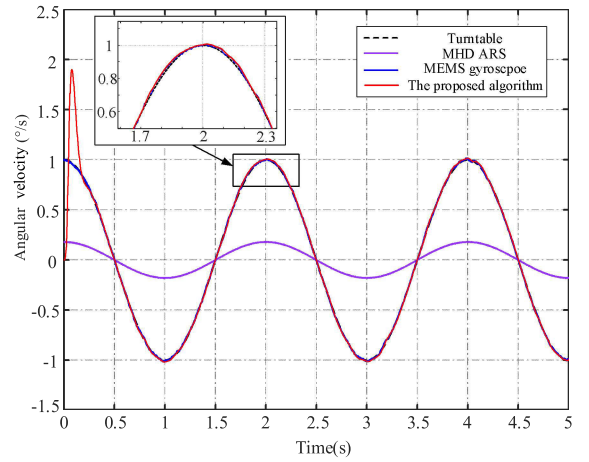

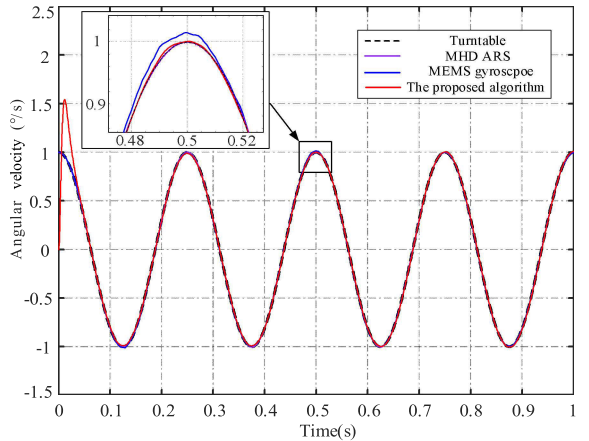Fig. 8.   0.5 Hz signal fusion results.

Fig. 9.   4 Hz signal fusion results.

To verify the effectiveness of the algorithm, we use the SHAKF algorithm to compare the fusion results. First, when measuring a 0.5 Hz signal, we optimize the SHAKF to an accurate state of fusion result by modifying the measurement noise variances of both sensors. Then we observe variations in fusion results as the signal frequency increases.

Based on the results presented in Fig. 11, when the signal frequency increases to 4 Hz, the SHAKF fusion result
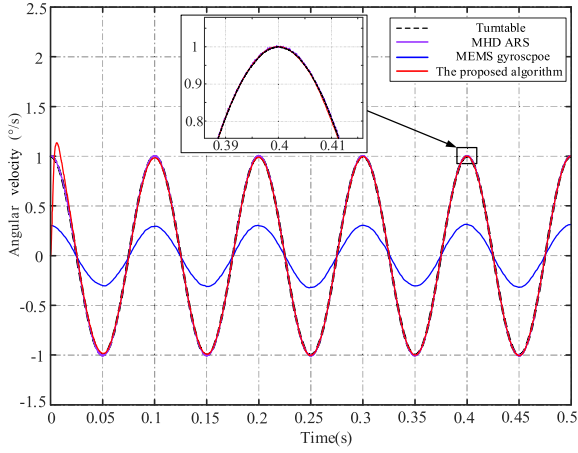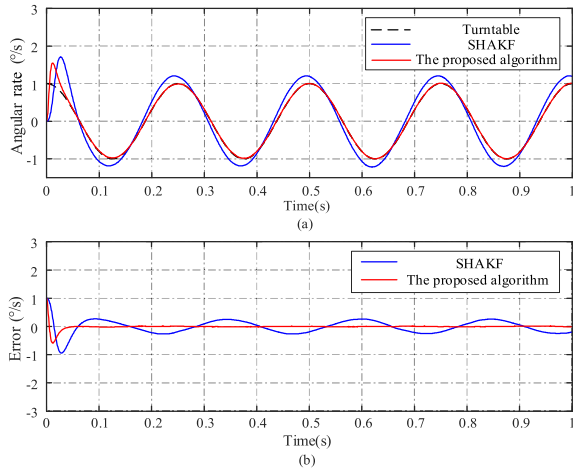
Fig. 10.   10 Hz signal fusion results.

Fig. 11.   Comparison of the 4 Hz signal fusion results. (a) Comparison of fusion results. (b) Comparison of errors.
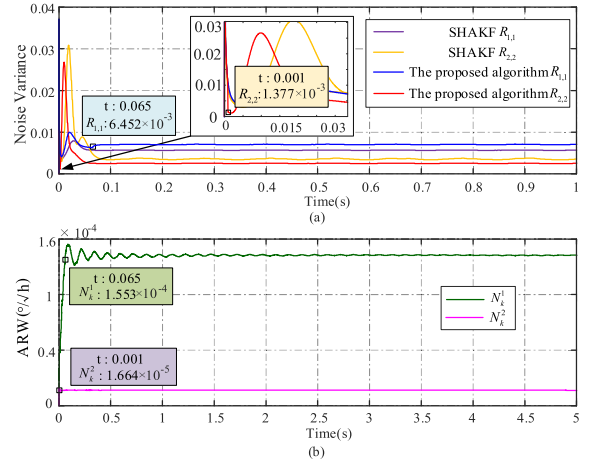

Fig. 12.   Update of the main diagonal elements of the measurement noise covariance for the 4 Hz signal. (a) Measurement noise variance update curves. (b) ARW coefficient update curves.

the fusion result for a 10 Hz signal is more accurate due to such a setup of the proposed algorithm.

Table II demonstrates the fusion effects of the two algorithms when the signal frequency varies. When the filter converges, the results of the root mean square error (RMSE) of the proposed algorithm are significantly smaller than those of the SHAKF. The accuracy of the SHAKF algorithm is significantly reduced by signal variation. The proposed algorithm modifies the measurement noise covariance matrix based on the ARW coefficients, which results in more adaptivity in handling the frequency variations of the measured signals.

E. Mixed-Frequency Signal Experiment

We further validate the effectiveness of the proposed algorithm using a mixed-frequency vibration signal. In the test, the mixed vibration signal consists of 0.5 and 10 Hz signals. These two frequencies cover the bands where the amplitude response of the two sensors is normal and attenuated, respectively, and give a good indication of how the algorithm works in the face of attenuation of the response of the components of the mixed signal. The angular amplitude of the 0.5 Hz signal is 5.555 mrad, and that of the 10 Hz signal is 50 μrad. The mixed signals resemble the narrow-band harmonic vibration characteristics of satellite platforms.

The results depicted in Fig. 13 demonstrate a notable attenuation of the response of the MHD ARS for the 0.5 Hz signal, as well as a significant attenuation of the response of the MEMS gyroscope for the 10 Hz signal accompanied by significant noise. The black frame in Fig. 13 illustrates the deviation of the fusion result (red line) from the turntable motion (black line) in some areas. This is because, although the MEMS gyroscope has a low-pass filter, it cannot eliminate low-frequency noise, which leads to a noisy measurement signal and impairs the accuracy of the fusion result.

In Fig. 14(b), the error of the proposed algorithm converges at 0°/s. According to the error curve of the SHAKF algorithm, the primary errors are present in the amplitude and phase estimation of the 0.5 Hz signal, which contributes to a significant error. The error curve of the proposed algorithm illustrates

experiences a significant error, while the proposed algorithm demonstrates convergence around 0°/s.

Fig. 12(a) shows the process of updating the measurement noise variances of both sensors. $R_{1,1}$ and $R_{2,2}$ are the diagonal elements of the measurement noise covariance matrix for the MEMS gyroscope and MHD ARS, respectively. Based on the two ARW coefficient variations illustrated in Fig. 12(b), the $R_{1,1}$ is modified at 0.065 s, and the $R_{2,2}$ is modified at 1 ms. As depicted in Fig. 12(a), the SHAKF algorithm trusts the measurement signal of the MHD ARS measurement signal close to the proposed algorithm. However, it still relies on the MEMS gyroscope measurement signal, resulting in phase and amplitude errors in the fused signal.

Relative to the SHAKF, the proposed algorithm has a higher convergence result for $R_{1,1}$ and a smaller convergence result for $R_{2,2}$. This indicates that the proposed algorithm adaptively modifies the measurement noise covariance based on the signal frequency, consequently adjusting the Kalman gain. The proposed algorithm relies more on the MHD ARS measurement signal and reduces the utilization of the MEMS gyroscope attenuation measurement signal. The fusion result for the 4 Hz signal is more accurate than the 0.5 Hz signal due to the smaller measurement noise of the MHD ARS. Similarly,

TABLE II
RMSE (°/S) OF FUSION RESULTS

Method	MEMS gyroscope	MHD ARS	SHAKF	The proposed algorithm
0.5Hz	0.0315	0.5650	0.0108	0.0098
4Hz	0.0120	0.0091	0.1831	0.0071
10Hz	0.4820	0.0085	0.3428	0.0039

Fig. 13. Mixed-frequency signal fusion results.
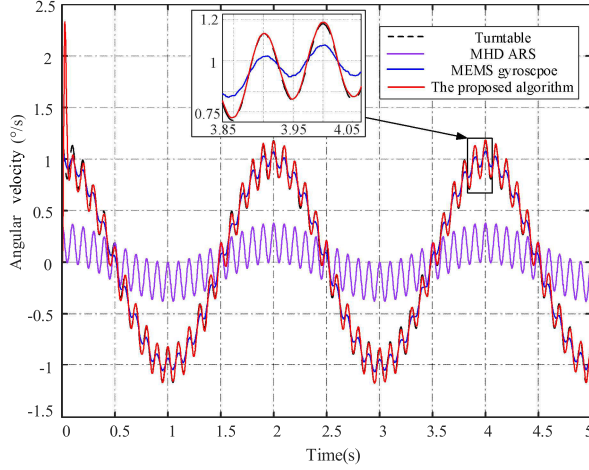
Fig. 14. Comparison of mixed-frequency signal fusion results. (a) Comparison of fusion results. (b) Comparison of errors.
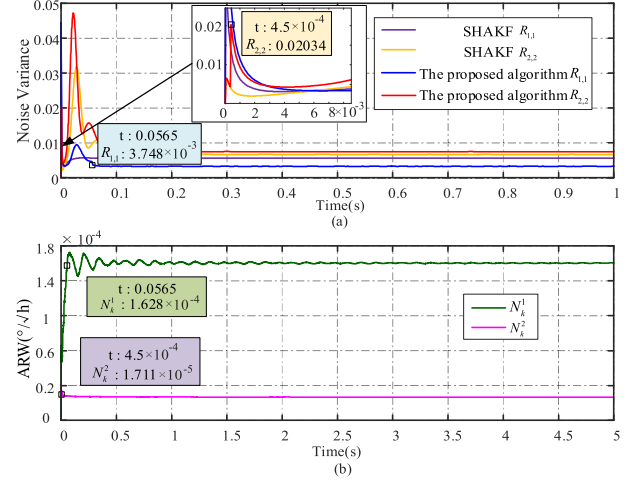

Fig. 15. Update of the main diagonal elements of the measurement noise covariance matrix for the mixed-frequency vibration signal. (a) Measurement noise variance update curves. (b) ARW coefficient update curves.
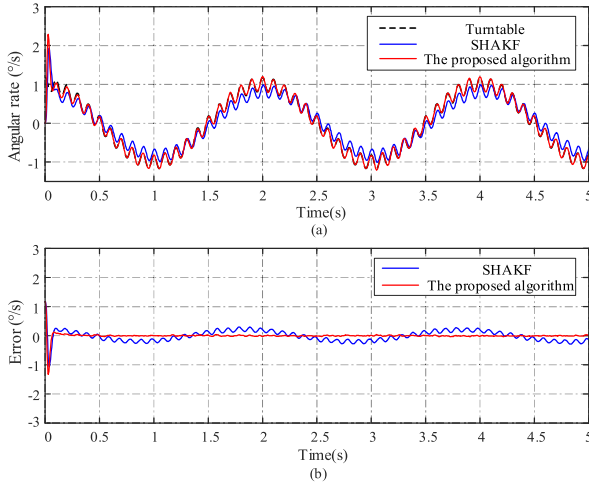
the ARW coefficients versus the signal frequency, which allows the algorithm to make better use of the 0.5 Hz signals from the MEMS gyroscope and obtains a more accurate angular rate estimation. In the test, when the filters converge, the RMSE of the SHAKF is 0.1482°/s and the RMSE of the proposed algorithm is 0.0143°/s.

V. CONCLUSION

Aiming at the problem of harmonic vibration measurement in laser beam stabilization control of free-space optical systems, this article proposes an adaptive Kalman filter based on online ARW estimation. The filter utilizes the measurement signals from the sensors to estimate the ARW coefficients online and adjusts the measurement noise covariance according to the relationship between the signal frequency and the ARW coefficients. Therefore, the method solves the problem of sensor amplitude response variation with frequency in data fusion. In the experiment, we tested three single-frequency vibration signals and a mixed-frequency vibration signal, respectively. The proposed algorithm can adaptively modify the measurement noise covariance matrix according to the frequency variation, thus adjusting the Kalman gain for the purpose of adjusting the utilization of the two sensor signals. Its RMSE is significantly smaller than that of the SHAKF algorithm. The fusion results of the proposed algorithm can reflect the real motion of the turntable.

The experimental results show that the proposed algorithm has a promising application in satellite platform vibration

that the trust of the filter in the two measurement signals is successfully adjusted, and the fusion result reflects the real motion of the turntable.

The process of updating the measurement noise variances in the proposed algorithm based on the variations of the two ARW coefficients is illustrated in Fig. 15. Compared to the SHAKF algorithm, the proposed algorithm has a smaller convergence result for $R_{1,1}$ and a larger convergence result of $R_{2,2}$. The adjustment improves the trust of the filter in the MEMS gyroscope measurement signal. As in the case of single-frequency signals, the proposed algorithm adaptively modifies the measurement noise covariance matrix based on

measurement. In the future, we will use the MEMS gyroscope with higher precision to obtain more accurate fusion results. Meanwhile, we will replace the turntable to establish the relationship between signal frequency and ARW coefficients under a wide bandwidth, and explore the fusion of vibration signals at higher frequencies.

REFERENCES

[1] G. D. Roumelas, H. E. Nistazakis, E. Leitgeb, A. N. Stassinakis, and G. S. Tombras, "On the performance of optical wireless communication links impaired by time jitter, M-turbulence and pointing errors," *Opt. Commun.*, vol. 472, Oct. 2020, Art. no. 126033.

[2] J. T. Valliyakalayil, A. J. H. Sutton, R. E. Spero, D. A. Shaddock, and K. McKenzie, "Enhanced frequency noise suppression for LISA by combining cavity and arm locking control systems," *Phys. Rev. D, Part. Fields*, vol. 105, no. 6, Mar. 2022, Art. no. 062005.

[3] M. Arikawa and T. Ito, "Performance of mode diversity reception of a polarization-division-multiplexed signal for free-space optical communication under atmospheric turbulence," *Opt. Exp.*, vol. 26, no. 22, p. 28263, 2018.

[4] Z.-Y. Xue, B. Qi, and G. Ren, "Vibration-induced jitter control in satellite optical communication," *Proc. SPIE*, vol. 8906, pp. 512–520, Aug. 2013.

[5] D. Jie, "Simulating the performance of ring-based coriolis vibrating gyroscopic sensors," *Microsyst. Technol.*, vol. 25, no. 1, pp. 139–149, Jan. 2019.

[6] D. R. Laughlin and D. Smith, "Development and performance of an angular vibration sensor with 1–1000 Hz bandwidth and nanoradian level noise," *Proc. SPIE*, vol. 4489, pp. 208–214, Jan. 2002.

[7] J. J. Scozzafava et al., "Design of a very small inertially stabilized optical space terminal," *Proc. SPIE*, vol. 6709, pp. 39–48, Sep. 2007.

[8] D. M. Boroson et al., "Overview and results of the lunar laser communication demonstration," *Proc. SPIE*, vol. 8971, pp. 213–223, Mar. 2014.

[9] D. M. Boroson, A. Biswas, and B. L. Edwards, "MLCD: Overview of NASA's Mars laser communications demonstration system," in *Proc. Free-Space Laser Commun. Technol. XVI*, San Jose, CA, USA, Jun. 2004, pp. 16–28.

[10] Y. Ji, X. Li, T. Wu, C. Chen, and S. Zhang, "Quantitative analysis method of error sources in magnetohydrodynamic angular rate sensor for structure optimization," *IEEE Sensors J.*, vol. 16, no. 11, pp. 4345–4353, Jun. 2016.

[11] T. Iwata, M. Uo, and T. Kawahara, "Ground-based precision attitude determination using repeated smoothing with sequential rate bias and attitude estimation," in *Proc. AIAA Guid., Navigat., Control Conf.*, Aug. 2010, p. 8451.

[12] T. Sun, F. Xing, Z. You, X. Wang, and B. Li, "Deep coupling of star tracker and MEMS-gyro data under highly dynamic and long exposure conditions," *Meas. Sci. Technol.*, vol. 25, no. 8, Aug. 2014, Art. no. 085003.

[13] S. Liang, Y. Huang, W. Zhu, and F. Zhao, "Effective nested Kalman fusion for improving microelectromechanical system array performance," *Meas. Sci. Technol.*, vol. 31, no. 11, Nov. 2020, Art. no. 115109.

[14] M. Narasimhappa, S. L. Sabat, and J. Nayak, "Fiber-optic gyroscope signal denoising using an adaptive robust Kalman filter," *IEEE Sensors J.*, vol. 16, no. 10, pp. 3711–3718, May 2016.

[15] T. Iwata, H. Hoshino, T. Yoshizawa, and T. Kawahara, "Precision attitude determination for the advanced land observing satellite (ALOS): Design, verification, and on-orbit calibration," in *Proc. AIAA Guid., Navigat. Control Conf. Exhib.*, Hilton Head, SC, USA, Aug. 2007, p. 6817.

[16] W. Ibrahim and B. Shankar, "MHD boundary layer flow and heat transfer of a nanofluid past a permeable stretching sheet with velocity, thermal and solutal slip boundary conditions," *Comput. Fluids*, vol. 75, pp. 1–10, Apr. 2013.

[17] Z. Wang, Z. Liu, K. Tian, and H. Zhang, "Frequency-scanning interferometry for dynamic measurement using adaptive sage-Husa Kalman filter," *Opt. Lasers Eng.*, vol. 165, Jun. 2023, Art. no. 107545.

[18] Y. Li, B. Hu, F. Qin, and K. Li, "Online estimation of ARW coefficient of fiber optic gyro," *Math. Problems Eng.*, vol. 2014, pp. 1–10, May 2014.

[19] Y. Su, C. Ma, J. Han, X. Wang, Y. Wang, and Z. Ji, "Research on magnetohydrodynamic angular rate sensor denoising for a space laser stabilization control system," *Appl. Sci.*, vol. 13, no. 10, p. 5895, May 2023.

[20] A. H. Mohamed and K. P. Schwarz, "Adaptive Kalman filtering for INS/GPS," *J. Geodesy*, vol. 73, no. 4, pp. 193–203, May 1999.